ARTICLE

doi:10.1038/nature10870

Crystal structure of the channelrhodopsin light-gated cation channel

Hideaki E. Kato[1], Feng Zhang[2], Ofer Yizhar[2], Charu Ramakrishnan[2], Tomohiro Nishizawa[1], Kunio Hirata[3], Jumpei Ito[4], Yusuke Aita[4], Tomoya Tsukazaki[1], Shigehiko Hayashi[5], Peter Hegemann[6], Andrés D. Maturana[4], Ryuichiro Ishitani[1], Karl Deisseroth[2] & Osamu Nureki[1]

Channelrhodopsins (ChRs) are light-gated cation channels derived from algae that have shown experimental utility in optogenetics; for example, neurons expressing ChRs can be optically controlled with high temporal precision within systems as complex as freely moving mammals. Although ChRs have been broadly applied to neuroscience research, little is known about the molecular mechanisms by which these unusual and powerful proteins operate. Here we present the crystal structure of a ChR (a C1C2 chimaera between ChR1 and ChR2 from *Chlamydomonas reinhardtii*) at 2.3 Å resolution. The structure reveals the essential molecular architecture of ChRs, including the retinal-binding pocket and cation conduction pathway. This integration of structural and electrophysiological analyses provides insight into the molecular basis for the remarkable function of ChRs, and paves the way for the precise and principled design of ChR variants with novel properties.

Organisms ranging from archaebacteria to human beings capture energy and/or information contained within environmental sources of light by using photoreceptors called rhodopsins, which consist of seven-transmembrane-helix proteins, called opsins, covalently linked to retinal. On the basis of primary sequences, the corresponding opsin genes are classified into two groups: microbial (type I) and animal (type II). Type I opsin genes are found in archaea, eubacteria, fungi and algae, whereas type II opsin genes are expressed in animals, including human beings. The type II proteins indirectly influence transmembrane ion currents by coupling to G-protein-based signal transduction pathways. In contrast, the type I proteins (not normally found in animals) include direct-light-activated regulators of transmembrane ion conductance, such as the light-driven ion pumps called bacteriorhodopsins and halorhodopsins (BRs and HRs)[1,2] and the light-driven ion channels ChRs[3]. The light-driven ion pumps have been extensively studied, and structure–function relationships are well known. As opposed to these ion pumps, very little is known about the structure of ChRs or the mechanism by which these seven-transmembrane proteins conduct cations in a light-dependent manner[3].

Beginning in 2005, it was found that ChRs could be expressed in mammalian neurons to mediate precise and reliable control of action potential firing in response to light pulses, without the need for exogenous retinal in vertebrate systems[4–9]. ChRs have now been used to control neuronal activity in a wide range of animals, resulting in insights into fundamental aspects of circuit function as well as dysfunction and treatment in pathological states[10,11]. However, despite the rapid progress of optogenetics (a technology also encompassing the use of ion pumps, such as HRs), virtually nothing is known about how a seven-transmembrane protein can form a light-switchable channel for cations. Although a rough helical arrangement was visible in the recently published ChR2 electron microscopy structure of two-dimensional crystals at 6 Å resolution, amino acid positioning and insights into channel function remained completely lacking[12]. A high-resolution three-dimensional image would be of enormous value, not only to enhance understanding of microbial opsin-based channels, but also to guide optogenetics in the generation of ChR variants with novel function related to spectrum, selectivity and kinetics. Even with limited structural models, ChR variants have been engineered with faster or extended open-state lifetimes[13–17], shifted absorption spectra[13,17,18], reduced desensitization[6,18–20], and increased expression and photocurrent magnitude[6,15–17,19]. These advances represent the tip of the iceberg in terms of what could be achieved for all of the above properties, as well as for altered ion selectivity and unitary (single-channel) conductance properties, if detailed structural knowledge could be obtained to facilitate true electrostatic calculations and molecular dynamics simulations.

Here we present the ChR crystal structure at 2.3 Å resolution. This high-resolution information, along with electrophysiological analyses, has revealed the fundamentals of ChR architecture and guides the way to a basic working model for channelrhodopsin function.

Overall ChR structure

ChR2 from *C. reinhardtii* consists of 737 amino acids; the seven transmembrane domains (TMs) and photocurrent functionality are all contained within the amino-terminal ~300 amino acids. To identify the most promising candidates for structural studies, we constructed and explored an extensive range of different ChRs and ChR chimaeras with distinct carboxy-terminal truncations. Using fluorescence-detection size-exclusion chromatography (FSEC)[21], we found that a novel chimaeric and truncated sequence termed C1C2, primarily consisting of ChR1 (ref. 3) without its C terminus and with the last two TMs swapped for those from ChR2 (related to previous chimaeras[19,20,22] but with an additional six-amino-acid modification of the C terminus, namely removal of the sequence NKGTGK), was not only expressed well in Sf9 insect cells but also showed good stability and monodispersity as well as similar spectral characteristics to previous chimaeras[22] (Supplementary Fig. 1). The crystals obtained from fully dark-adapted C1C2 in the lipidic cubic phase belonged to the $C222_1$ space group and diffracted X-rays to 2.3 Å resolution. We solved the C1C2 structure by the multiple anomalous dispersion (MAD)

[1]Department of Biophysics and Biochemistry, Graduate School of Science, The University of Tokyo, 2-11-16 Yayoi, Bunkyo-ku, Tokyo 113-0032, Japan. [2]Department of Bioengineering and Howard Hughes Medical Institute, Stanford University, Stanford, California 94305, USA. [3]RIKEN SPring-8 Center, Hyogo 679-5148, Japan. [4]Bioengineering Department, Nagaoka University of Technology, Niigata 940-2188, Japan. [5]Department of Chemistry, Graduate School of Science, Kyoto University, Kyoto 606-8502, Japan. [6]Institute of Biology, Experimental Biophysics, Humboldt-University, Invalidenstrae 42, D-10115 Berlin, Germany.

method, using mercury-derivatized crystals (Supplementary Fig. 2). As far as we know, this is the first example of the phase determination by MAD for the crystal obtained in the lipidic cubic phase.

The truncated C1C2 chimaera (residues 1–342) is composed of an N-terminal extracellular domain (N domain, residues 24–83, marked in Fig. 1a, d), the seven TMs (TM1–TM7; residues 84–317) connected by three cytoplasmic loops (ICL1–ICL3) and three extracellular loops (ECL1–ECL3), and the C-terminal intracellular domain (C domain, residues 318–356) (Fig. 1b, d). In addition to the region spanning the N-terminal residues 1–23, which is processed as a signal peptide (data not shown), residues 24–48, 110–117 and 343–356 are structurally disordered and invisible in the electron density map, whereas the core transmembrane region is clearly resolved (Fig. 1a). Searches of the Protein Data Bank using the Dali server (http://ekhidna.biocenter.helsinki.fi/dali) suggested that the N domain, consisting of a short 3_{10}-helix and two β-strands, has a novel fold. Within each C1C2 protomer, 6 lipids and 43 water molecules were observed.

Two C1C2 protomers were found to be tightly associated into a closely apposed dimer, as previously predicted from electron microscopy[12]. Interfacial interactions occur in the N domain, ECL1, TM3 and TM4 of each molecule (Fig. 1b, c). Notably, Cys 66 (27), Cys 73 (34) and Cys 75 (36) in the N domain (ChR2 numbering is shown in parentheses here and below for comparison with earlier literature) form three disulphide bonds between protomers. As Cys 73 and Cys 75 are highly conserved in ChRs, this interaction may contribute to stabilizing the N-domain interaction and molecular dimerization (Supplementary Fig. 3).

Structural comparison with BR

We next compared the C1C2 structure with that of BR and bRh (bovine rhodopsin). The primary sequence of ChR is similar to that of BR as well as other microbial opsins, such as xanthorhodopsin and sensory rhodopsin II (Supplementary Fig. 4). Consistent with this sequence similarity, C1C2 superimposed well on BR (PDB accession 1IW6)[23], but not on bRh (PDB accession 3C9L)[24] (Fig. 1d and Supplementary Fig. 5). TM3–6 between C1C2 and BR are very similar, and the position of the protonated Schiff base is conserved (Fig. 1e), whereas there are three distinct features between the two structures. First, C1C2 has additional N-terminal and C-terminal domains. The N domain, as noted above, contributes to dimer formation, and the C domain may be involved in subcellular localization and scaffolding in *Chlamydomonas*; for example, to tether ChR to the algal eyespot[25]. Second, TM7 of C1C2 protrudes into the intracellular space, projecting ~18 Å from the membrane surface, and the intracellular end of TM7 is shifted towards the central axis of the monomer by 2.7 Å, as compared with BR (Fig. 1d). Although the function of this protruding part of TM7 is unclear, His 313, His 317 and Gly 318 may contribute to stabilizing the intracellular C domain via a water-mediated hydrogen-bonding network (Supplementary Fig. 6). Last, and most importantly, the C1C2 extracellular ends of TM1 and TM2 are tilted outward by 3.0 Å and 4.1 Å, respectively, compared to those of BR (Fig. 1e). These tilts enlarge the cavity formed by TM1, 2 and 7 and allow water influx for a cation-translocation pathway, as discussed later.

Retinal-binding pocket, Schiff base and counterion

As in other microbial-type rhodopsins, all-*trans* retinal (ATR) is covalently bound to Lys 296 (257) on TM7 (Lys 216 in BR), forming the Schiff base. As in BR, five aromatic residues (Trp 163, Phe 217, Trp 262, Phe 265 and Phe 269) are located around the polyene chain and the β-ionone ring, forming a hydrophobic pocket for ATR (Fig. 2a, b), whereas Cys 167 (128), Thr 198 (159) and Ser 295 (256) form a less-hydrophobic pocket, and may contribute to colour shift (Fig. 2a, b).

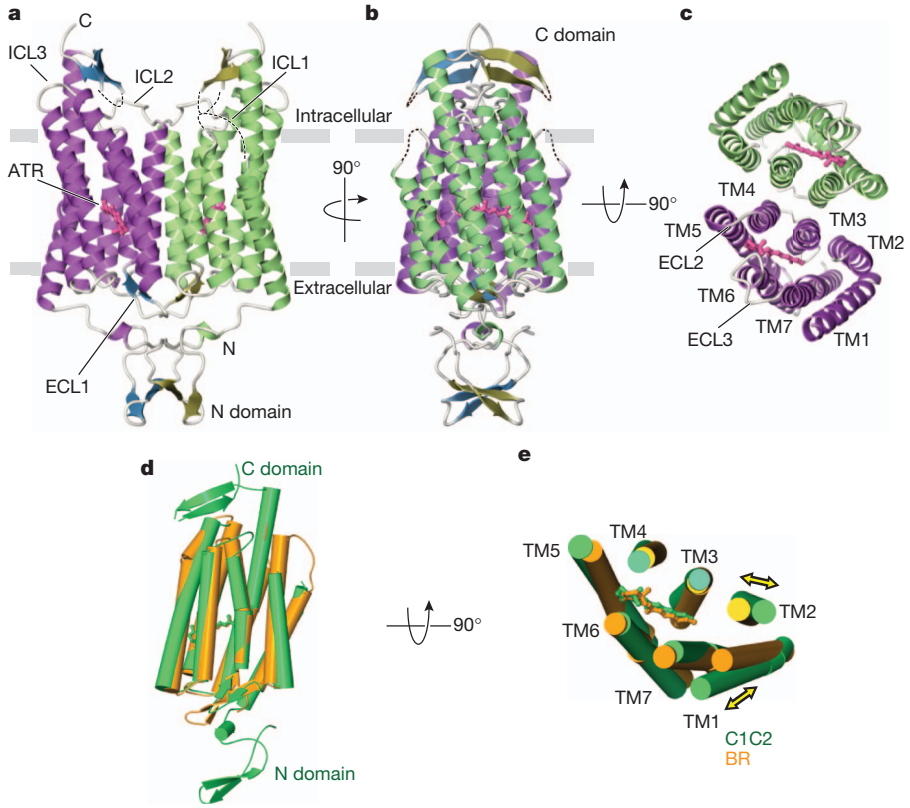

Figure 1 | Structure of C1C2 and comparison with BR. **a**–**c**, Crystal structure of the C1C2 dimer, viewed parallel to the membrane from two angles (**a**, **b**), and viewed from the extracellular side (**c**). C1C2 consists of the N domain, the seven transmembrane helices (TM1–TM7) connected by extracellular loops (ECL1–ECL3) and intracellular loops (ICL1–ICL3), and the C domain. Disordered regions are represented as dotted lines. The ATR is coloured pink. **d**, **e**, Side view (**d**) and extracellular view (**e**) of the superimposed TMs of C1C2 (green) and BR (orange). The yellow double arrows indicate the shifts of the extracellular parts of TM1 and TM2.

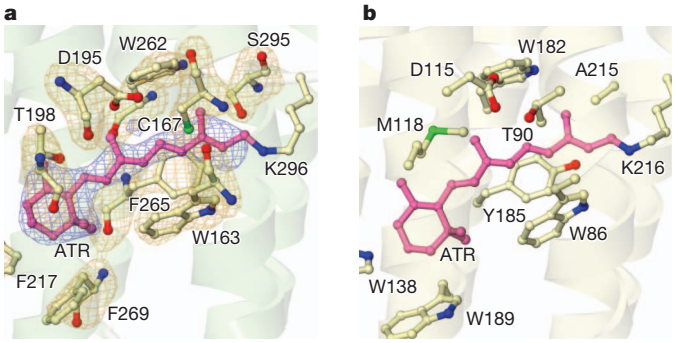

Figure 2 | Structural comparison of the retinal-binding pocket between C1C2 and BR. **a**, Structure of the retinal-binding pocket of C1C2, with an omit map of ATR at 3σ and of the surrounding residues (subtract 39 from the C1C2 residue number to obtain ChR2 numbering) at 3.5σ. **b**, Structure of the retinal-binding pocket of BR.

A previous report suggested that the side chains of Cys 167 (128) and Asp 195 (156) (Thr 90 and Asp 115 in BR) directly hydrogen bond with each other[26] (Fig. 2a), and that this interaction may function as the molecular switch to direct transition to the conducting state. However, in the present C1C2 structure, the distances between the thiol group of Cys 167 and the carboxyl oxygen atoms of Asp 195 are 4.4 Å and 4.6 Å, respectively, and the thiol group of Cys 167 is not associated with Asp 195, but with the π-electron system in the retinal molecule (Fig. 2a).

In BR, a water molecule receives a proton from the protonated Schiff base and donates a proton to Asp 85 (ref. 27; Fig. 3b); this arrangement is conserved in C1C2. However, in C1C2 the distances from the protonated Schiff base are 4.4 Å, 3.4 Å and 3.0 Å respectively for the water molecule, Glu 162 (123) (Asp 85 in BR) and Asp 292 (253) (Asp 212 in BR) (Fig. 3a, b). Therefore, in C1C2, Asp 292 or possibly Glu 162, but not the water located between them, may directly receive a proton from the protonated Schiff base. In BR, Asp 212 retains a low pK_a because it is hydrogen bonded to Tyr 57 and Tyr 185, which do not move during the photocycle (Fig. 3b). On the other hand, in C1C2, Tyr 57 and Tyr 185 are substituted with Phe 133 and Phe 265, and Asp 292 only forms a hydrogen bond with water (Fig. 3a); thus Asp 292 could move relatively freely in the photocycle. Therefore, in C1C2, the pK_a of Asp 292 can change, in contrast to the corresponding residue in BR. Moreover, the pK_a values of Glu 162 and Asp 292, calculated using PROPKA[28] (Supplementary Table 2), showed that Glu 162 may be protonated and Asp 292 may be deprotonated in our structure. Thus, we suggest that Asp 292, rather than Glu 162, is the primary proton acceptor in C1C2, consistent with the finding that Glu 123 mutants show current amplitudes similar to wild type[13,17]. To verify further this notion, we expressed the E162A and D292A mutants of C1C2 in HEK293 cells, and recorded photocurrents in response to 465-nm light pulses (Fig. 3c, d and Supplementary Figs 7 and 8), revealing that replacement of Glu 162 by alanine resulted in moderately decreased currents, whereas the substitution of Asp 292 by alanine almost completely abolished photocurrents despite robust membrane expression. Moreover, the onset time constant (τ_{ON}) of the D292A mutant was significantly larger than that of wild type (Supplementary Fig. 9), consistent with the structure showing that Asp 292, rather than Glu 162, may be the major proton acceptor from the protonated Schiff base in ChR.

Electronegative pore framed by four TM helices

We calculated the electrostatic surface potential of C1C2, which revealed an electronegative pore formed by TM1, 2, 3 and 7 (Fig. 4a). In this pathway, a number of negatively charged residues, including Glu 129 (90), Glu 136 (97) and Glu 140 (101), as well as Glu 162 (123) and Asp 292 (253), are aligned along the pore (Fig. 4b). Because most of the negatively charged residues are derived

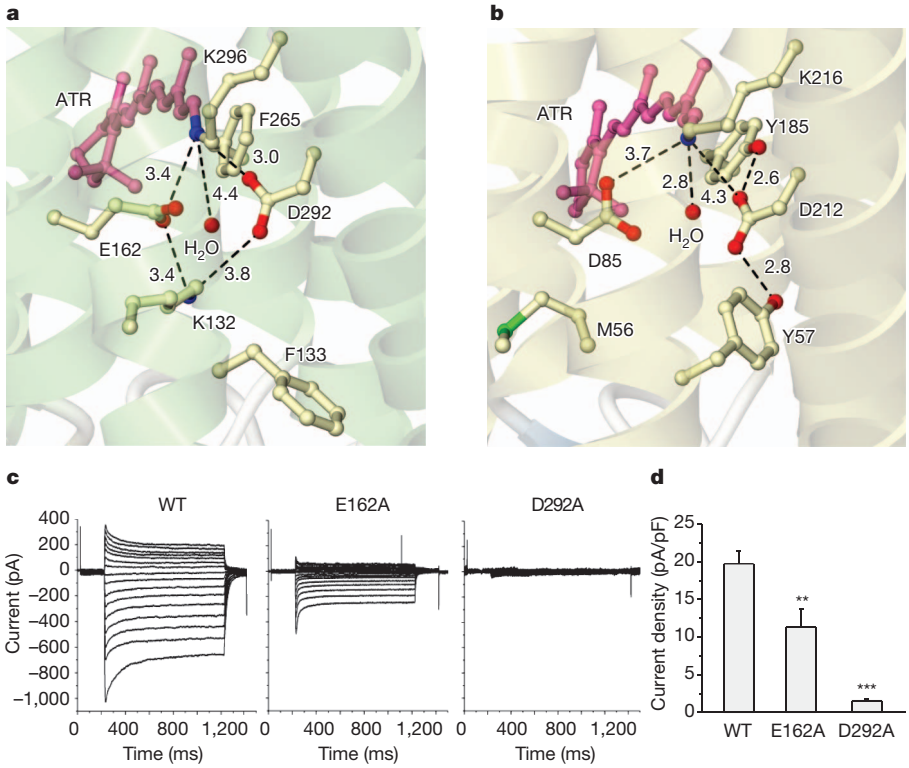

Figure 3 | The protonated Schiff base and its counterions in C1C2 and BR. **a**, **b**, Structures of the environment around the Schiff base in C1C2 (**a**) and BR (**b**). Numbers indicate the distance between two atoms connected by dashed lines. **c**, Effects of the mutation of two possible counterions on the photocurrent. Photocurrents on C1C2-expressing HEK293 cells were measured at 16 different holding potentials. WT, wild type. **d**, The peak amplitudes of the photocurrents, normalized by the cell's input capacitance. Values are means and s.e.m. of 7–15 experiments. $^{**}P < 0.01$, $^{***}P < 0.001$.

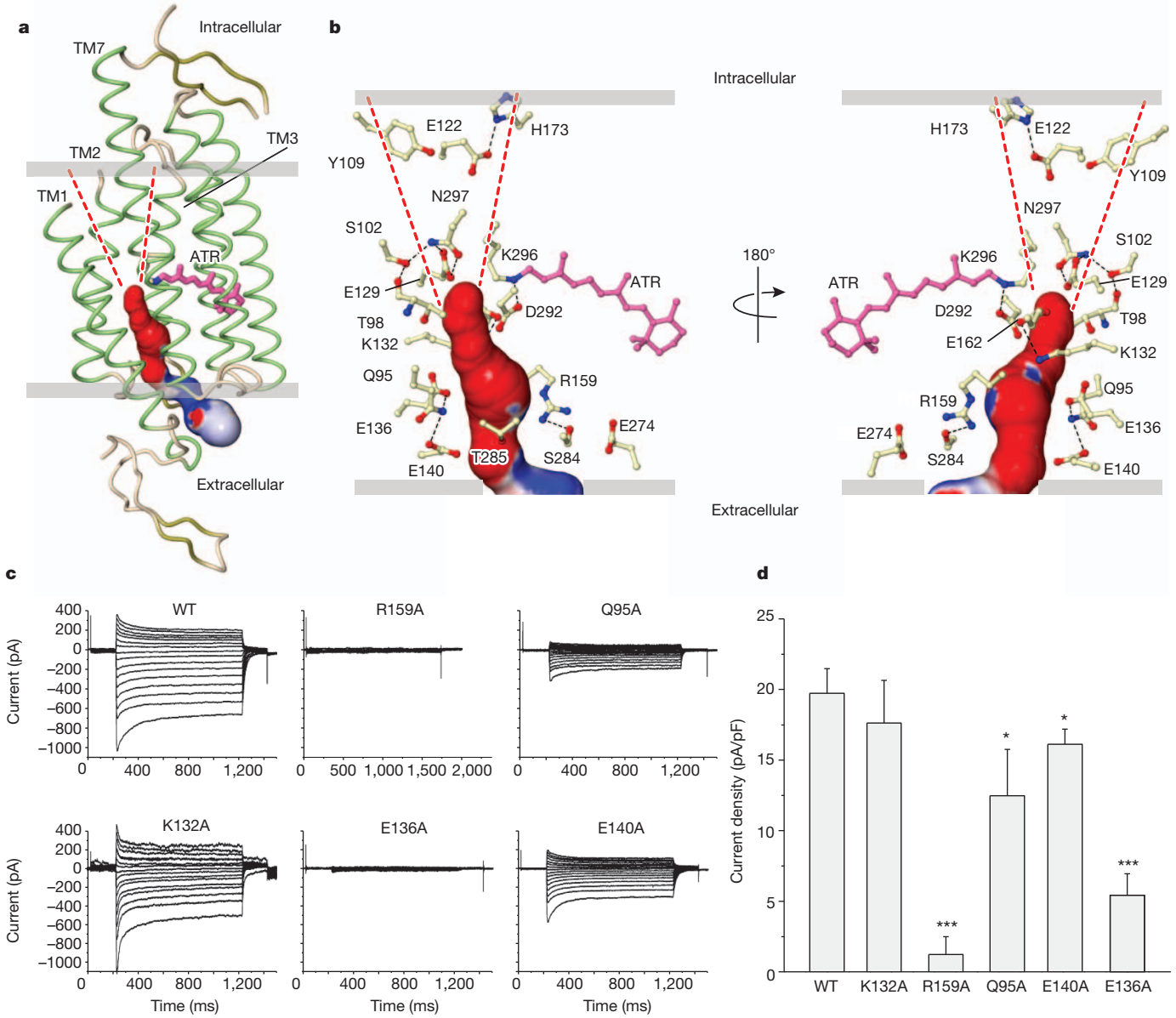

Figure 4 | Cation-conducting pathway formed by TM1, 2, 3 and 7. a, Pore-lining surface calculated by the CAVER[37] program, coloured by the electrostatic potential. Dashed red lines indicate putative intracellular vestibules. **b**, Close-up views of the surface of the pore, with the 17 polar lining residues (subtract 39 from the C1C2 residue number to obtain ChR2 numbering). Hydrogen bonds are shown as black dashed lines. **c**, Photocurrents of mutants of the five residues within the pathway, measured under the same conditions as in Fig. 3c. **d**, The peak amplitudes of the photocurrents, as in Fig. 3d. $*P < 0.05$, $***P < 0.001$. Error bars represent s.e.m.

from TM2, we suggest that the ion conductance and selectivity of C1C2 are mainly defined by TM2.

On the extracellular side of the pore, a vestibule formed by the N domain and ECL1–3 opens up to a diameter of about 8 Å, where Lys 154 (115), Lys 209 (170) and Arg 213 (174) form a slightly electropositive surface around the vestibule (Supplementary Fig. 10). Deeper within the vestibule, Arg 159 (120), Tyr 160 (121), Glu 274 (235) and Ser 284 (245) form a weak electronegative surface and fix the positions of TM3, 6 and 7 by a water-mediated hydrogen-bond network (Supplementary Fig. 11a). As these four residues are highly conserved not only in ChRs but also in BRs (Arg 82, Tyr 83, Glu 194 and Glu 204, respectively), and the corresponding residues in BR reportedly have an important role in proton pumping, we generated the R159A mutant in C1C2. We found that this mutant did not produce a photocurrent despite robust membrane expression (Fig. 4c, d and Supplementary Figs 7 and 8); because the orientation of Arg 159 is quite different from the corresponding Arg residue in BR, and these residues form the extracellular hydrophilic surface, we suggest that this conserved cluster has an important role in creation of the extracellular vestibule, rather than in proton movement as in BR (Supplementary Fig. 11b).

In the middle of the pore, 12 polar residues (Gln 95 (56), Thr 98 (59), Ser 102 (63), Glu 122 (83), Glu 129 (90), Lys 132 (93), Glu 136 (97), Glu 140 (101), Glu 162 (123), Thr 285 (246), Asp 292 (253) and Asn 297 (258)) form a hydrophilic and strongly electronegative surface (Fig. 4b). To investigate contributions to ChR function, we measured photocurrents, kinetics and selectivity for four mutants (Q95A, K132A, E136A, E140A) (Fig. 4c, d and Supplementary Figs 7–9 and 12). The K132A mutant had faster kinetics and similar current amplitude relative to wild type, whereas the Q95A and E140A mutants exhibited moderately reduced currents, and the E136A mutant showed very little photocurrent, despite robust membrane expression. Three of the four mutants (Q95A, K132A and E136A) altered ion selectivity (Supplementary Fig. 12); therefore, we suggest that this

pore is important for cation conduction and that, as previously suggested[29], Glu 136 (97) is essential.

Although this putative cation-conducting pathway is opened towards the extracellular side, the cytoplasmic side of this pathway is occluded owing to two constrictions (Figs 4b and 5). The first constriction is formed by three highly conserved polar residues: Ser 102 (63), Glu 129 (90) and Asn 297 (258) (Figs 4b and 5a). In this constriction site, Ser 102, with a β-OH group that hydrogen bonds to the main-chain carbonyl oxygen of Thr 98, fixes the position of Asn 297 and, in turn, Asn 297 fixes Glu 129 by hydrogen bonds. Glu 129 protrudes into and occludes the pore. To analyse this putative channel gate, we prepared four mutants (S102D, E129A, E129Q and N297D) and measured photocurrents, kinetics and ion selectivity (Supplementary Figs 7–9, 12 and 13). We found that E129A, E129Q and N297D affect ion selectivity and S102D, E129Q and N297D affect channel kinetics (Supplementary Figs 9 and 12). These results, consistent with previous work[30,31], indicate the importance of these three residues and suggest that cations pass through this constriction site in the conducting state.

The second constriction is formed by the phenol group of Tyr 109 (70) (Figs 4b and 5b). Given the high *B*-factor of the C-terminal end of TM1 (Supplementary Fig. 14) and a previous Fourier transform infrared spectroscopy (FT-IR) study showing that the α-helices undergo conformational changes during the photocycle[32], movement of the TM1 C-terminal end may open the pore exit formed between TM1, 2 and 7. As TM1 does not directly interact with the retinal chromophore, the signal of retinal isomerization is expected to be transmitted to TM1 via movements of TM2, 3 and/or 7. However, we cannot exclude the possibility that movements of TM2, 3 and/or 7 form a cytoplasmic vestibule next to Tyr 109, and further studies will be required to identify the pore exit.

Discussion

This first crystal structure of a light-gated cation channel in the closed/dark state at 2.3 Å resolution provides insight into ChR dimerization, retinal binding and cation conductance. Moreover, owing to the large N domain unique to ChR, it has been difficult to align precisely the ChR sequence with other microbial rhodopsins (notably BR), and the present structure-based alignment (Supplementary Fig. 4) will assist in the design and interpretation of functional analyses, including electrophysiological and spectroscopic studies of ChR at the molecular level.

The structural features around the ATR, Schiff base, and conduction pathway also provide insight into the blueshifted absorption spectrum of ChR (λ_{max} = 470 nm), as compared to that of BR (λ_{max} = 568 nm). In general, the maximum absorption wavelength of retinal proteins is determined by the energy difference between ground (S_0) and excited (S_1) states, and this gap is mainly affected by the planarity of the conjugated system of the retinal chromophore, the distance between the protonated Schiff base and its counterion, and the interaction of the chromophore with polar or polarizable residues[33]. Although the planarity of the ATR is unchanged between ChR and BR, the counterion of ChR, Asp 292, is located ~1 Å closer to the Schiff base than the corresponding Asp residue of BR (Fig. 3a, b), and the negatively charged residues are aligned along the conducting pathway (Fig. 4a, b). These environments are likely to stabilize the S_0 state of ChR, thus enlarging the energy gap between the S_0 and S_1 states and thereby causing the relative absorption spectrum blueshift.

Much about the photocycle remains unknown but is thought to be similar to that of BR[31,34,35], in which the essential early event is the dipole change of the protonated Schiff base, which alters the nitrogen pK_a by several orders of magnitude. In the case of ChRs, this may cause the release of the Schiff base proton to Asp 292 (probably not to either Glu 162 or water because Asp 292 is closer than these other two moieties, which also may explain why the D292A mutant is inactive; Fig. 3). The protonation of Asp 292 is likely to repel Lys 132 (93), as with Arg 82 in BR, and this movement may enlarge pore diameter and help cations to pass (Figs 3a and 4b). It is also thought that channel opening may be coupled with reprotonation of the Schiff base. Given the calculated pK_a (Supplementary Table 2) and the distance from the Schiff base nitrogen atom, we suggest two candidates for this proton donor—Glu 122 and Glu 129 (Supplementary Fig. 15)—but further studies, including structural determinations of photocycle intermediate states, will be required to refine our model.

In recent years, many strategies have been applied to create ChR variants with improved properties for optogenetics, ranging from designer ChR variants based on functional and structural similarities between BR and ChR (E123X, H134R, C128X, I131V, D156A, T159C, C1V1)[6,13–15,17,19,36], to chimaera construction along with mutagenesis (ChRGR, L132C, ChD, ChEF, C1V1)[16–19] (Fig. 6a). These approaches have generated a number of ChR variants with useful properties, but the high-resolution crystal structure is a prerequisite for the design of ChR variants with ideal properties. The present crystal structure describes the environment around the retinal-binding pocket (Fig. 6a, b), which will enable optimized design of red- and blueshifted ChR variants. In addition, structure of the cation-conducting pathway may facilitate construction of ChR variants with improved photocurrents, photosensitivity, cation selectivity and kinetics. For example, K132A and Q95A show strong photocurrents and K^+ selectivity (Supplementary Figs 9 and 12), which could be useful to suppress neural activity.

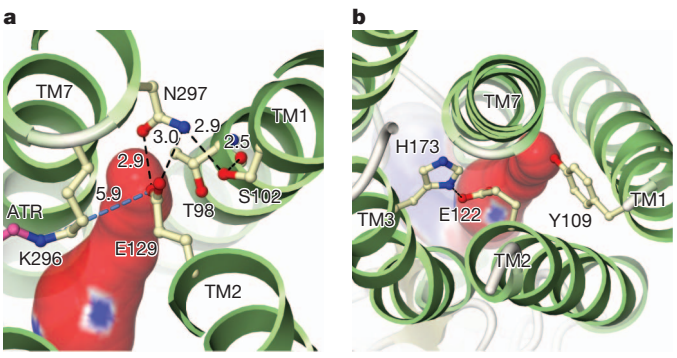

Figure 5 | Two constriction sites on the cytoplasmic side of C1C2 in the closed state. a, The first constriction site is formed by Ser 102 (63), Glu 129 (90) and Asn 297 (258). Hydrogen bonds are shown as black dashed lines. The blue dashed line represents a possible proton transfer pathway. **b**, The second constriction, made by Tyr 109. The cavity formed by TM1, 2 and 7 is occluded by Tyr 109, and the cavity formed by TM2, 3 and 7 is occluded by Glu 122 and His 173.

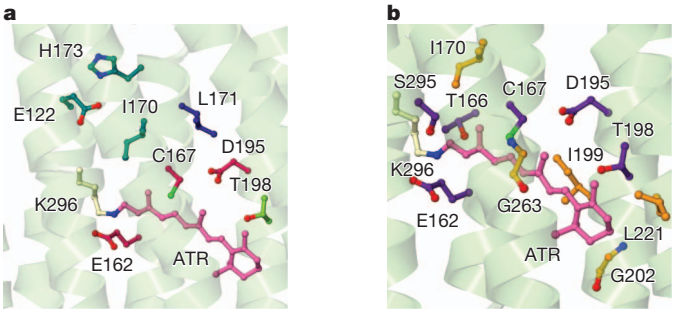

Figure 6 | Distribution of known mutations and possible candidates for future mutations. a, Mutations that affect both the absorption spectrum and the kinetics (Cys 167 (128), Glu 162 (123) and Asp 195 (156); deep red), the conductance (Thr 198 (159); light green), the selectivity (Leu 171 (132); dark blue) and the kinetics (Glu 122 (83), Ile 170 (131) and His 173 (134); dark cyan) of ChR2. **b**, Polar (Glu 162 (123), Thr 166 (127), Cys 167 (128), Asp 195 (156), Thr 198 (159) and Ser 295 (256); magenta) and non-polar (Ile 170 (131), Ile 199 (160), Gly 202 (163), Leu 221 (182) and Gly 263 (224); orange) residues surrounding ATR.

To understand the photocycle in more detail, further structural studies, including determination of crystal structures in intermediate states, are clearly needed. However, the present structural information represents a key step in enabling the principled design of ChR variants with new properties, and will accelerate both applications of optogenetics to intact-systems biology, and basic mechanistic understanding of these remarkable photoreceptor proteins.

METHODS SUMMARY

C1C2 was cloned into cleavable enhanced green fluorescent protein (EGFP)–His_8 fusion pFastBac1 vector. The fusion protein was expressed in insect cells, solubilized in 2.5% (w/v) *n*-dodecyl-β-D-maltoside (DDM) and 0.5% (w/v) cholesteryl hemisuccinate, and purified by nickel affinity chromatography. After that, the C-terminal EGFP was cleaved by His-tagged tobacco etch virus (TEV) protease (homemade). Then the sample mixture was passed through Ni-NTA resin again to remove the cleaved His-tagged EGFP and TEV protease. The sample was further purified by size-exclusion chromatography. Crystals were grown in a lipidic cubic phase using monoolein. Diffraction data were measured at beamline X06SA of the Swiss Light Source and at beamline BL32XU of SPring-8. The structure was solved by the MAD method using mercury derivative. Data collection and refinement statistics are presented in Supplementary Table 1. Electrophysiological recordings were conducted using patch-clamp on HEK293 cells expressing the wild-type and mutant C1C2.

Full Methods and any associated references are available in the online version of the paper at www.nature.com/nature.

Received 28 October 2011; accepted 3 January 2012.
Published online 22 January 2012.

1. Oesterhelt, D. & Stoeckenius, W. Rhodopsin-like protein from the purple membrane of *Halobacterium halobium*. *Nat. New Biol.* **233,** 149–152 (1971).
2. Matsuno-Yagi, A. & Mukohata, Y. Two possible roles of bacteriorhodopsin; a comparative study of strains of *Halobacterium halobium* differing in pigmentation. *Biochem. Biophys. Res. Commun.* **78,** 237–243 (1977).
3. Nagel, G. *et al.* Channelrhodopsin-1: a light-gated proton channel in green algae. *Science* **296,** 2395–2398 (2002).
4. Boyden, E. S., Zhang, F., Bamberg, E., Nagel, G. & Deisseroth, K. Millisecond-timescale, genetically targeted optical control of neural activity. *Nature Neurosci.* **8,** 1263–1268 (2005).
5. Li, X. *et al.* Fast noninvasive activation and inhibition of neural and network activity by vertebrate rhodopsin and green algae channelrhodopsin. *Proc. Natl Acad. Sci. USA* **102,** 17816–17821 (2005).
6. Nagel, G. *et al.* Light activation of channelrhodopsin-2 in excitable cells of *Caenorhabditis elegans* triggers rapid behavioral responses. *Curr. Biol.* **15,** 2279–2284 (2005).
7. Ishizuka, T., Kakuda, M., Araki, R. & Yawo, H. Kinetic evaluation of photosensitivity in genetically engineered neurons expressing green algae light-gated channels. *Neurosci. Res.* **54,** 85–94 (2006).
8. Bi, A. *et al.* Ectopic expression of a microbial-type rhodopsin restores visual responses in mice with photoreceptor degeneration. *Neuron* **50,** 23–33 (2006).
9. Zhang, F., Wang, L. P., Boyden, E. S. & Deisseroth, K. Channelrhodopsin-2 and optical control of excitable cells. *Nature Methods* **3,** 785–792 (2006).
10. Yizhar, O., Fenno, L. E., Davidson, T. J., Mogri, M. & Deisseroth, K. Optogenetics in neural systems. *Neuron* **71,** 9–34 (2011).
11. Fenno, L., Yizhar, O. & Deisseroth, K. The development and application of optogenetics. *Annu. Rev. Neurosci.* **34,** 389–412 (2011).
12. Muller, M., Bamann, C., Bamberg, E. & Kuhlbrandt, W. Projection structure of channelrhodopsin-2 at 6 Å resolution by electron crystallography. *J. Mol. Biol.* **414,** 86–95 (2011).
13. Gunaydin, L. A. *et al.* Ultrafast optogenetic control. *Nature Neurosci.* **13,** 387–392 (2010).
14. Berndt, A., Yizhar, O., Gunaydin, L. A., Hegemann, P. & Deisseroth, K. Bi-stable neural state switches. *Nature Neurosci.* **12,** 229–234 (2009).
15. Berndt, A. *et al.* High-efficiency channelrhodopsins for fast neuronal stimulation at low light levels. *Proc. Natl Acad. Sci. USA* **108,** 7595–7600 (2011).
16. Kleinlogel, S. *et al.* Ultra light-sensitive and fast neuronal activation with the Ca^{2+}-permeable channelrhodopsin CatCh. *Nature Neurosci.* **14,** 513–518 (2011).
17. Yizhar, O. *et al.* Neocortical excitation/inhibition balance in information processing and social dysfunction. *Nature* **477,** 171–178 (2011).
18. Wen, L. *et al.* Opto-current-clamp actuation of cortical neurons using a strategically designed channelrhodopsin. *PLoS ONE* **5,** e12893 (2010).
19. Lin, J. Y., Lin, M. Z., Steinbach, P. & Tsien, R. Y. Characterization of engineered channelrhodopsin variants with improved properties and kinetics. *Biophys. J.* **96,** 1803–1814 (2009).
20. Wang, H. *et al.* Molecular determinants differentiating photocurrent properties of two channelrhodopsins from *Chlamydomonas*. *J. Biol. Chem.* **284,** 5685–5696 (2009).
21. Kawate, T. & Gouaux, E. Fluorescence-detection size-exclusion chromatography for precrystallization screening of integral membrane proteins. *Structure* **14,** 673–681 (2006).
22. Tsunoda, S. P. & Hegemann, P. Glu 87 of channelrhodopsin-1 causes pH-dependent color tuning and fast photocurrent inactivation. *Photochem. Photobiol.* **85,** 564–569 (2009).
23. Matsui, Y. *et al.* Specific damage induced by X-ray radiation and structural changes in the primary photoreaction of bacteriorhodopsin. *J. Mol. Biol.* **324,** 469–481 (2002).
24. Stenkamp, R. E. Alternative models for two crystal structures of bovine rhodopsin. *Acta Crystallogr. D* **64,** 902–904 (2008).
25. Mittelmeier, T. M., Boyd, J. S., Lamb, M. R. & Dieckmann, C. L. Asymmetric properties of the *Chlamydomonas reinhardtii* cytoskeleton direct rhodopsin photoreceptor localization. *J. Cell Biol.* **193,** 741–753 (2011).
26. Nack, M. *et al.* The DC gate in Channelrhodopsin-2: crucial hydrogen bonding interaction between C128 and D156. *Photochem. Photobiol. Sci.* **9,** 194–198 (2010).
27. Lanyi, J. K. Proton transfers in the bacteriorhodopsin photocycle. *Biochim. Biophys. Acta* **1757,** 1012–1018 (2006).
28. Bas, D. C., Rogers, D. M. & Jensen, J. H. Very fast prediction and rationalization of pK_a values for protein–ligand complexes. *Proteins* **73,** 765–783 (2008).
29. Sugiyama, Y. *et al.* Photocurrent attenuation by a single polar-to-nonpolar point mutation of channelrhodopsin-2. *Photochem. Photobiol. Sci.* **8,** 328–336 (2009).
30. Ruffert, K. *et al.* Glutamate residue 90 in the predicted transmembrane domain 2 is crucial for cation flux through channelrhodopsin 2. *Biochem. Biophys. Res. Commun.* **410,** 737–743 (2011).
31. Plazzo, A. P. *et al.* Bioinformatic and mutational analysis of channelrhodopsin-2 cation conducting pathway. *J. Biol. Chem.* http://dx.doi.org/10.1074/jbc.M111.326207 (2011).
32. Radu, I. *et al.* Conformational changes of channelrhodopsin-2. *J. Am. Chem. Soc.* **131,** 7313–7319 (2009).
33. Lasogga, L., Rettig, W., Otto, H., Wallat, I. & Bricks, J. Model systems for the investigation of the opsin shift in bacteriorhodopsin. *J. Phys. Chem. A* **114,** 2179–2188 (2010).
34. Ritter, E., Stehfest, K., Berndt, A., Hegemann, P. & Bartl, F. J. Monitoring light-induced structural changes of Channelrhodopsin-2 by UV-visible and Fourier transform infrared spectroscopy. *J. Biol. Chem.* **283,** 35033–35041 (2008).
35. Bamann, C., Kirsch, T., Nagel, G. & Bamberg, E. Spectral characteristics of the photocycle of channelrhodopsin-2 and its implication for channel function. *J. Mol. Biol.* **375,** 686–694 (2008).
36. Bamann, C., Gueta, R., Kleinlogel, S., Nagel, G. & Bamberg, E. Structural guidance of the photocycle of channelrhodopsin-2 by an interhelical hydrogen bond. *Biochemistry* **49,** 267–278 (2010).
37. Petřek, M. *et al.* CAVER: a new tool to explore routes from protein clefts, pockets and cavities. *BMC Bioinformatics* **7,** 316 (2006).

Supplementary Information is linked to the online version of the paper at www.nature.com/nature.

Acknowledgements We thank Y. Tanaka, T. Higuchi, M. Hattori and H. Nishimasu for useful discussions; T. Hino for technical support; and the beamline staff members at BL32XU of SPring-8 (Hyogo, Japan) and at X06SA of the Swiss Light Source (Villigen, Switzerland) for technical help during data collection. This work was supported by the Japan Society for the Promotion of Science (JSPS) through its "Funding Program for World-Leading Innovative R&D on Science and Technology (FIRST program)" to O.N., by a grant for the National Project on Protein Structural and Functional Analyses from the Ministry of Education, Culture, Sports, Science and Technology (MEXT) to O.N., and by a Grant-in-Aid for Scientific Research (S) from MEXT to O.N. F.Z. is supported by the McKnight Foundation. K.D. is supported by the Gatsby Charitable Foundation and the Keck, Snyder, Woo, and Yu Foundations, as well as by the National Institutes of Health, and the Defense Advanced Research Project Agency Reorganization and Plasticity to Accelerate Injury Recovery (DARPA REPAIR) program.

Author Contributions H.E.K. performed the structural determination of C1C2, prepared the mutants, measured the spectral property of C1C2 and wrote the paper. A.D.M. performed the electrophysiological analyses of C1C2. J.I. helped A.D.M. to take pictures of C1C2 and to determine membrane expression. Y.A. helped A.D.M. to perform patch-clamp experiments. T.T., T.N., R.I. and O.N. assisted with the structural determination. K.H. assisted with the data collection of C1C2. O.N., F.Z. and K.D. conceived the study; F.Z., O.Y. and K.D. helped to organize the project; S.H. and P.H. provided input on structural considerations; and C.R. with K.D. constructed the final C1C2 that enabled crystal structure determination. All authors discussed the results and commented on the manuscript. O.N. and K.D. supervised all aspects of the work and wrote/edited the manuscript.

Author Information Data have been deposited at the Protein Data Bank under accession number 3UG9. Reprints and permissions information is available at www.nature.com/reprints. The authors declare no competing financial interests. Readers are welcome to comment on the online version of this article at www.nature.com/nature. Correspondence and requests for materials should be addressed to O.N. (nureki@biochem.s.u-tokyo.ac.jp) or K.D. (deissero@stanford.edu).

METHODS

Expression and purification of C1C2. Chimaeras between ChR1 and ChR2 from *C. reinhardtii* and other algal species were subcloned into the pCGFP-EU vector[21] for expression in HEK293 cells. The tobacco etch virus (TEV) protease cleavage site, the coding sequence of enhanced GFP (EGFP), and the octa-histidine tag ($EGFP\text{-}His_8$) were introduced at the C terminus of the chimaeric constructs. All constructs were screened by FSEC analysis[21]. The gene encoding the best chimaera (C1C2) was subcloned into the modified pFastBac1 vector for expression in Sf+ insect cells. Baculovirus-infected Sf+ cells were cultured in Sf900II (Invitrogen) at 27 °C for 24 h, and then the temperature was reduced to 20 °C. Cells were harvested 72 h after infection by centrifugation at 6,000*g* for 10 min. The pellets were disrupted by two passages through a microfluidizer at 15,000 pounds per square inch, and were resuspended in a buffer containing 300 mM NaCl, 50 mM Tris-HCl, pH 8.0, 5% glycerol and 0.1 mM phenylmethylsulfonyl fluoride (PMSF). The cell debris was cleared by centrifugation at 10,000*g* for 40 min, and the crude membrane fraction was collected by ultracentrifugation (Ti45 rotor, 43,000 r.p.m., 1 h). This fraction was solubilized in a buffer containing 300 mM NaCl, 50 mM Tris-HCl, pH 8.0, 5% glycerol, 20 mM imidazole, 0.1 mM PMSF, 2.5% *n*-dodecyl-β-D-maltoside (DDM) and 0.5% cholesteryl hemisuccinate (CHS). The insoluble material was removed by ultracentrifugation (Ti70 rotor, 45,000 r.p.m., 30 min), and the supernatant was mixed with Ni-NTA resin (QIAGEN). After binding for 1 h, C1C2 was eluted in buffer supplemented with 300 mM imidazole. Following the cleavage of $EGFP\text{–}His_8$ by His-tagged TEV protease (homemade), the sample was reloaded onto the Ni-NTA column to remove the cleaved $EGFP\text{–}His_8$. The flow-through containing C1C2 was collected, concentrated, and further purified by size-exclusion chromatography in 150 mM NaCl, 50 mM Tris-HCl, pH 8.0,
5% glycerol, 0.05% DDM and 0.01% CHS. Peak fractions were pooled and concentrated to $\sim$10 mg ml^{-1} for crystallization. For the mercury derivative, the concentrated protein was incubated with a sixfold molar excess of methyl mercury chloride at 20 °C for 1 h. The derivative was ultracentrifuged and used for crystallization experiments.

Crystallization. C1C2 was mixed with monoolein (Sigma) in a 2:3 protein to lipid ratio (w/w). Aliquots (100 nl) of the protein-LCP mixture were spotted on a 96-well sandwich plate and overlaid by 1 µl of precipitant solution by the crystallization robot, mosquito LCP (TTP LabTech). Native crystals were obtained in 30–34% (w/v) PEG500DME, 100 mM Na citrate, pH 6.0, 100 mM $MgCl_2$, 100 mM NaCl and 100 mM $(NH_4)_2SO_4$, whereas the derivative crystals were grown in 31% (w/v) PEG500DME, 100 mM HEPES-NaOH, pH 7.0, 200 mM Li_2SO_4 and 10 mM ATP. All crystals were incubated for 2–3 weeks in the dark. They were harvested using micromounts (MiTeGen), and were flash-cooled in liquid nitrogen without any additional cryoprotectant.

Structure determination. X-ray diffraction data sets for the native and mercury-derivatized protein crystals were collected on beamline X06SA at SLS and beamline BL32XU at SPring-8, using a 1-µm-wide, 15-µm-high microbeam[38]. Data were indexed and scaled with the programs XDS[39] and SCALA[40], or with DENZO and SCALEPACK from the HKL2000 program suite (HKL Research). Experimental phases were determined by the MAD method, using the four Hg sites identified with the program SHELX[41]. Subsequent refinements of the heavy atom parameters and phase calculations were performed with the program SHARP[42]. The data collection and phasing statistics are shown in Supplementary Table 1. The initial model structure of C1C2 was built with the program Phyre[43], using the *Anabaena* sensory rhodopsin structure (PDB accession 1XIO) as the template. The resultant structure was manually modified to fit into the experimental electron density maps, using the program Coot[44]. The structure was then refined with the program Phenix[45]. Figures were prepared with Cuemol (http://www.cuemol.org).

Electrophysiology. HEK293 cells were cultured on poly-lysine-coated, glass-bottom culture dishes (Matsunami), and were transfected with 0.5 µg of a plasmid construct containing the GFP-tagged C1C2 or the GFP-tagged C1C2 mutants. At 24–30 h after transfection, the cells were placed in a bath medium, containing 140 mM NaCl, 1 mM $CaCl_2$, 2 mM $MgCl_2$ 10 mM HEPES and 5 mM glucose (pH 7.4 with NaOH), under an inverted microscope (Olympus IX71). Calcium and potassium photocurrents were measured by replacing 140 mM NaCl by 90 mM $CaCl_2$ or 140 mM KCl accordingly. For proton photocurrents, cell bath was 5 mM NaCl, 135 mM *N*-methyl-D-glucamine, 1 mM $CaCl_2$, 2 mM $MgCl_2$, 10 mM HEPES and 5 mM glucose (pH 6.4). A borosilicate patch pipette (Harvard Apparatus), with a resistance of about 5–8 MΩ, was filled with 140 mM KCl, 5 mM EGTA, 2 mM $MgCl_2$ and 10 mM HEPES (pH 7.2 with KOH). C1C2 currents were recorded in the voltage-clamp mode and in the whole-cell configuration. The cells were held at a membrane potential of −80 mV, and were depolarized by 10 mV voltage steps of 1.8 s up to +70 mV. The light-dependent currents were activated 200 ms after the depolarization step, with 465 nm light (1.5 mW mm^{-2}) for 1,000 ms, elicited by a high power LED illumination system (LEX2-B, Brainvision) connected to an A/D converter (Digidata 1440, Axon CNS, Molecular Devices), controlled by the pClamp10 software (Axon CNS). The light power was 1.5 mW mm^{-2}. Currents were measured using an Axopatch 200B amplifier (Axon CNS, Molecular Devices), filtered at 2 KHz, and sampled at 5 KHz, using a Digidata 1440A digitizer (Axon CNS) controlled by the pClamp10 software (Axon CNS).

Fluorescence measurements. The cells were transfected with 0.5 µg wild-type C1C2 or C1C2 mutants, using Fugene 6, for 30 h. The cells were then washed with PBS and fixed with 4% paraformaldehyde in PBS for 20 min at room temperature (20 °C), and washed again with PBS before microscopy observation. GFP fluorescence was observed with a laser confocal microscope (FV1000 Olympus). To estimate membrane expression of C1C2 and its mutants, the ratio between the membrane fluorescence and cytosolic were determined.

Ultraviolet/visible spectroscory. Ultraviolet/visible absorption spectra were recorded with an Ultrospec 3300 pro ultraviolet/visible spectrophotometer (Amersham Biosciences) by use of 1-cm quartz cuvettes. Freshly prepared C1C2 was used for the measuments. pH was adjusted by addition of 100 volumes of buffer solution yielding final concentrations of 50 mM Na citrate, pH 4.0, 50 mM Na acetate, pH 5.0, 50 mM Na cacodylate, pH 6.0, 50 mM HEPES, pH 7.0, 50 mM Tris, pH 8.0 and 9.0, or 50 mM CAPS, pH 10.0, plus 150 mM NaCl, 5% glycerol, 0.05% DDM and 0.01% CHS.

38. Hirata, K. *et al.* New micro-beam beamline at SPring-8, targeting at protein microcrystallography. *AIP Conference Proceedings* **1234,** 893–896 (2010).
39. Kabsch, W. XDS. *Acta Crystallogr. D* **66,** 125–132 (2010).
40. Evans, P. Scaling and assessment of data quality. *Acta Crystallogr. D* **62,** 72–82 (2006).
41. Schneider, T. R. & Sheldrick, G. M. Substructure solution with SHELXD. *Acta Crystallogr. D* **58,** 1772–1779 (2002).
42. de La Fortelle, E. & Bricogne, G. Maximumlikelihood heavy-atom parameter refinement for multiple isomorphous replacement and multiwavelength anomalous diffraction methods. *Methods Enzymol.* **276,** 472–494 (1997).
43. Kelley, L. A. & Sternberg, M. J. Protein structure prediction on the Web: a case study using the Phyre server. *Nature Protocols* **4,** 363–371 (2009).
44. Emsley, P., Lohkamp, B., Scott, W. G. & Cowtan, K. Features and development of Coot. *Acta Crystallogr. D* **66,** 486–501 (2010).
45. Adams, P. D. *et al.* PHENIX: a comprehensive Python-based system for macromolecular structure solution. *Acta Crystallogr. D* **66,** 213–221 (2010).